

Heavy-element damage seeding in proteins under XFEL illumination

Spencer K. Passmore*

*School of Physics, University of Melbourne, Parkville, Victoria 3010, Australia and
Optical Sciences Centre, Swinburne University of Technology, Hawthorn, Victoria 3122, Australia*

Alaric L. Sanders

*T.C.M. Group, Cavendish Laboratory, University of Cambridge, Cambridge CB3 0HE, United Kingdom and
School of Physics, University of Melbourne, Parkville, Victoria 3010, Australia*

Andrew V. Martin

School of Science, STEM College, RMIT University, Melbourne, Victoria 3000, Australia

Harry M. Quiney

School of Physics, University of Melbourne, Parkville, Victoria 3010, Australia

Serial femtosecond X-ray crystallography (SFX) captures the structure and dynamics of biological macromolecules at high spatial and temporal resolutions. The ultrashort pulse produced by an X-ray free electron laser (XFEL) ‘outruns’ much of the radiation damage that impairs conventional crystallography. However, the rapid onset of ‘electronic damage’ due to electron ionization limits this benefit. Here, we distinguish the influence of different atomic species on the electronic damage to protein crystals in SFX by employing a plasma code that tracks the unbound electrons as a continuous energy distribution. The simulations show that trace quantities of heavy atoms ($Z > 10$) contribute a substantial proportion of global radiation damage by inducing electron ionization processes that are highly damaging on the XFEL pulse timescale. Native sulfur atoms have a considerable effect on damage-induced noise. Likewise, proteins suffer less damage when the crystal solvent contains lower concentrations of heavy elements. The proximity of the X-ray energy to a heavy-element absorption edge has a strong and non-trivial influence on the damage induced in these models. In one representative protein (lysozyme substituted with selenomethionine), adjusting the X-ray energy from 14 keV to 12 keV is as effective at reducing the ionization of light atoms as compressing the pulse width from 50 fs to 5 fs. These results indicate that relatively small quantities of heavy elements can substantially affect global radiation damage in the XFEL regime.

I. INTRODUCTION

Serial femtosecond crystallography (SFX) is a potentially revolutionary structural determination tool for biology that overcomes key challenges faced by conventional X-ray crystallography [1]. Using X-ray free electron lasers (XFELs) to serially illuminate small crystals with ultrabright, femtosecond pulses of radiation, a molecule’s structural signal is captured so swiftly that the atomic nuclei are effectively frozen in place [2–4]. This approach not only mitigates structural damage, allowing for the use of much higher fluences, but also facilitates time-resolved crystallography. As such, SFX can be applied to capture molecular movies of rapid biological processes, including photoactivated dynamics [5–11] and enzyme catalysis [12–14].

In the ideal limit of SFX, the X-ray diffraction pattern of each crystal is captured by an ultrashort pulse before any secondary damage processes can propagate [15–19]. In this ‘diffraction before destruction’ picture, damage no longer constrains the X-ray intensities that allow for

successful structure determination. This freedom allows for structure determination from micron or sub-micron crystals [3, 20]. Indeed, several XFEL experiments have captured the structures of radiation-sensitive metalloproteins without evidence of significant structural deformation [4, 7, 20]. The technique can thus be applied to molecules that do not readily form large crystals, such as membrane proteins [1, 21–24]. Using smaller crystals is particularly advantageous for time-resolved experiments, which demand larger quantities of sample than static structure determination [9], are less tolerant to beam attenuation, and benefit from high crystal surface area to volume ratios when attempting to induce structural changes chemically [25].

In practice, however, ultrafast electronic processes disrupt the simple diffract-and-destroy picture – scattering signals seen in experiments generally remain dose-dependent even at the practical minimum pulse widths achievable (~ 10 fs) [17, 26–28]. In particular, the electrons ejected through photoionization and subsequent Auger decays initiate electron impact ionization (EII) cascades that will go on to become the main cause of ionization well before the end of the pulse [3, 29]. This ‘electronic damage’ has complex, non-linear effects on the scattered wavefield [26, 30–32], and various theoretical treatments have been proposed to model the underlying

* spencerpassmore@swin.edu.au

ultrafast damage processes [29–34]. Efficient use of limited XFEL beamtime [21, 35] therefore often depends on identifying experimental parameters that minimize electronic damage [36].

Heavy atoms ($Z > 10$ in this context) are ubiquitous in protein crystals. Though they typically comprise less than 1% of the illuminated atoms, they play a key role in the biochemistry of metalloproteins. Additionally, their unusual scattering behavior has various applications to X-ray crystallography. Anomalous phasing, a notable example, has been successfully extended to SFX with microcrystals using sulfur native to proteins [37–39], or with much heavier atoms deliberately added for a stronger signal [40–42] (as in Fig. 1). The rapid ionization of heavy atoms under high fluences induces a strong time dependence in their atomic scattering factors. This behavior is central to proposed methods of high-intensity radiation-damage-induced phasing (HI-RIP) [3, 27, 43–49].

A large part of the existing body of work dedicated to simulating atomic dynamics under XFEL illumination follows either the Monte Carlo molecular dynamics (MD) paradigm [28, 50–52] or a plasma approach [33, 53, 54]. These frameworks are in some sense complementary; the former provides a detailed picture of damage on the local scale, while the latter focuses on global statistics [49]. In the MD case, individual ions and electrons are treated as classical particles and tracked through space. Such modeling is too computationally demanding for system sizes over 100–1000 atoms, so cannot simulate typically sized proteins in full [27, 32, 34, 55]. In contrast, models that incorporate a zero-dimensional plasma code may capably simulate much larger (or arbitrary) systems [33, 49, 53, 56], mitigating possible difficulties in capturing the effect of trace elements.

Several plasma codes that treat the free electrons out of thermal equilibrium have been applied in studies of single-element targets [34, 54, 57–59]. However, all plasma codes used to simulate the damage sustained by biomolecules model the free electrons in local thermal equilibrium (LTE) with a Maxwellian energy distribution. This treatment may miss important effects – existing work on single-element, solid-density targets quotes thermalisation times in picoseconds [34, 57, 58, 60–62].

In this work, we present a plasma physics code with a non-LTE continuum model of the electron energy distribution and, using this code, examine electronic damage in protein crystals containing heavy elements without assuming instantaneous thermalization. We combine a custom-built frozen-shell Hartree-Fock code [63] with a non-standard B-spline approach to solving the Boltzmann equation for the time-dependent non-equilibrium energy distribution of the free electrons. The details of this framework are given in Sec. II. We apply the model to compare how light and heavy atoms influence the ionization dynamics of biological matter in Sec. III. Sec. IV identifies how trace quantities of heavy elements in biomolecular targets give rise to species-dependent

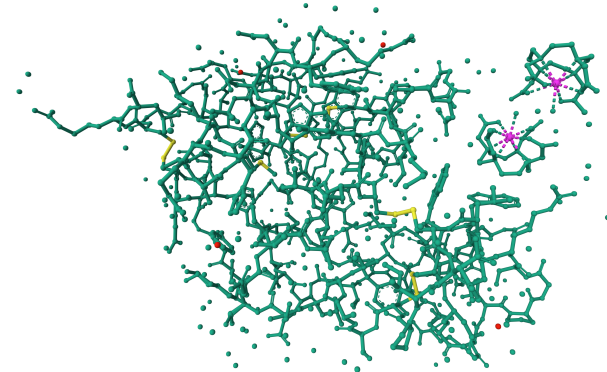


FIG. 1. Three possible structural sources of heavy atoms in the immediate environment of a crystallized protein. Shown is a refined structure for lysozyme.Gd (PDB id: 1H87 [64–66]). Sulfur atoms (yellow) are distributed heterogeneously through the lysozyme unit cell, chlorine ions (red) are present in the interstitial solvent, and gadolinium ions (magenta) are attached artificially.

high-damage regions of the pulse parameter space. After reporting on how the presence and composition of the solvent may affect these dynamics in Sec. V, we go on to identify new possible avenues for mitigating the impact of damage on structure determination in Sec. VI.

II. SIMULATION METHOD

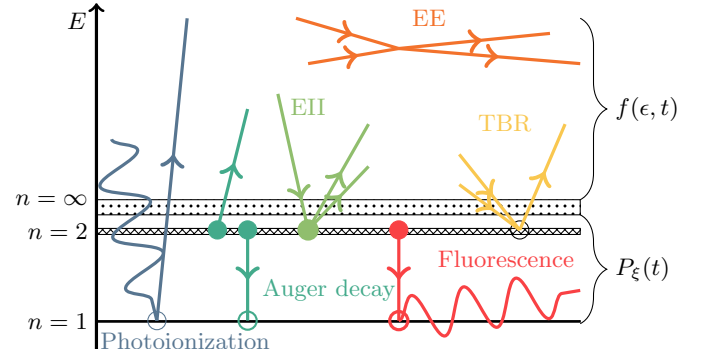


FIG. 2. Bound-free, bound-bound, and free-free transitions in biomolecular plasma. Bound energy levels are reminiscent of carbon for illustrative purposes. Processes are labeled to indicate the populations they affect: one or both of P (the ionic states) and f (the free electrons). The dotted section at $E = 0$ represents the weakly-bound molecular structure that is ignored here. Filled circles represent initial-state bound electrons, and hollow circles their final states.

In a typical XFEL experiment, it is change of ionic state, rather than nuclear motion, that makes up the bulk of the radiation damage [2, 27, 32]. It follows that a simulation of an XFEL target that correctly estimates

the time-dependent distribution of ion states will capture the most important part of the damage dynamics. We therefore approach the XFEL dynamics problem from the plasma physics perspective previously used in the study of metal plasmas [57–61].

This work uses a new version of the collisional-radiative plasma physics code AC4DC [33], which has been extended to couple the non-local thermal equilibrium (non-LTE) electron gas to the ion plasma. The code is optimized to model the plasma dynamics of low- Z matter in the XFEL regime, treating the constituent atoms as independent ions coupled to a bath of free electrons and the driving XFEL photons.

The model couples the time-dependent energy distribution of the free electrons, $f(\epsilon, t)$, to the population of possible ionic states, $P_\xi(t)$, through the processes of photoionization, Auger and fluorescent decay, electron impact ionization (EII), three-body recombination (TBR), and pairwise Coulomb electron-electron interactions. These processes are summarized in Fig. 2. Atomic parameters are calculated in the radially-averaged Hartree-Fock approximation [33, 63]. EII and TBR are approximated using the well-established binary-encounter dipole model of Kim and Rudd [67]. The equations of motion, obtained from radially averaging the Boltzmann equation, then read

$$\frac{\partial}{\partial t} f(\epsilon, t) = \mathcal{Q}[P_\xi, f](\epsilon) \quad (1)$$

$$\frac{d}{dt} P_\xi(t) = \sum_{\eta \neq \xi} \Gamma_{\eta \rightarrow \xi} P_\eta(t) - \Gamma_{\xi \rightarrow \eta} P_\xi(t), \quad (2)$$

where \mathcal{Q} and Γ represent the couplings to processes affecting f and P , respectively (illustrated in Fig. 2). Details for the calculations of the atomic cross-sections, Γ , are given in Ref. [63]. Explicit expressions for \mathcal{Q} are given in Appendix A.

We discretize the free electron distribution using an adaptive-grid spline expansion, in which $f(\epsilon)$ is expanded in piecewise-polynomial B-splines $B_k(\epsilon)$ [68]. These basis functions have compact support, allowing for efficient computations of the second- and third-order \mathcal{Q} tensors without sacrificing differentiability of f . As the simulation progresses, the spline grid is dynamically transformed to have an increased knot density in regions with complex energy-space structure, such as the vicinities of the thermal and photoelectron peaks (see Appendix A for further details). This adaptive grid allowed the code to perform full dynamical non-equilibrium plasma simulations of lysozyme in ~ 1 hour on a contemporary desktop.

The code achieved excellent agreement with published Monte-Carlo simulations by `ddcMD` of amorphous carbon [34] for the evolution of the ionic states and free electrons, and predicted similar ionic state dynamics to simulations by `XMDYN` of a glycine crystal [32, 50]. Somewhat surprisingly, the code also sees good agreement with the particle-in-cell DFT code `PICLS` [57] when modeling aluminium plasma for both the ion and free electron populations.

III. HEAVY-SEEDED IONIZATION CASCADES – LYSOZYME.GD

We first study the impact of heavy atoms in a representative model system – gadolinium-derivative hen egg-white lysozyme (lysozyme.Gd, derived from PDB entry 4ET8 [17, 69]) – subjected to a 15 fs FWHM Gaussian pulse of fluence $1.75 \times 10^{12} \text{ } 7.112 \text{ keV ph} \cdot \mu\text{m}^{-2}$. This protein derivative contains 2 Gd^{3+} ions and 10 S atoms in each asymmetric unit of ~ 1000 atoms. Three ‘toy’ variants of this system were simulated: lysozyme.Gd, non-derivative (Gd-free) lysozyme, and lysozyme with sulfur atoms substituted for nitrogen (the ‘light-atom control’). By contrasting the damage in these three materials, the effect of the heavy atoms on the dynamics may be inferred. The presence of water was neglected in these simulations; each system was modeled as a continuous, homogeneous material with the atomic composition of the protein – see Sec. V for an examination of the influence of the solvent within the protein crystal.

Figure 3(a) shows snapshots of the electron distributions of the systems during the pulse. Though S and Gd hold only a small fraction of the electrons in the lysozyme.Gd system, it may be readily seen that their photoelectrons hold a substantial fraction of the free electrons’ energy, comparable to that held by the light-atom photoelectrons. This is a direct consequence of the Z^4 dependence of photoabsorption cross-sections on atomic number [70]. The photoelectron peaks remain sharp for a substantial part of the pulse (up to $\sim t = 0$), emphasizing the necessity of the non-LTE treatment.

The inset plots in Fig. 3(a) show lysozyme.Gd with approximately twice the population of thermal electrons as the light-atom control. The vast majority of the additional electrons come from extra secondary ionization events in the *light* atoms. This is reflected by Fig. 3(b), which shows that the carbon 2s and 2p orbitals deplete much more rapidly when S and Gd are present in the system.

Figure 4 shows the heavy elements in lysozyme.Gd substantially elevate the degradation of the diffraction pattern due to the additional electronic damage suffered by the light atoms (see Fig. S3 for the effect on the atomic form factors). The diffraction pattern was computed by integrating snapshots of lysozyme’s light atom structure, with each atom’s electronic configuration, and thus scattering profile, stochastically chosen with weightings according to the bound state probability distribution of the plasma simulation (see Appendix A). We considered a single-protein diffraction pattern to highlight the impact of damage on the underlying signal without the need for assumptions on crystal size, morphology, and quality.

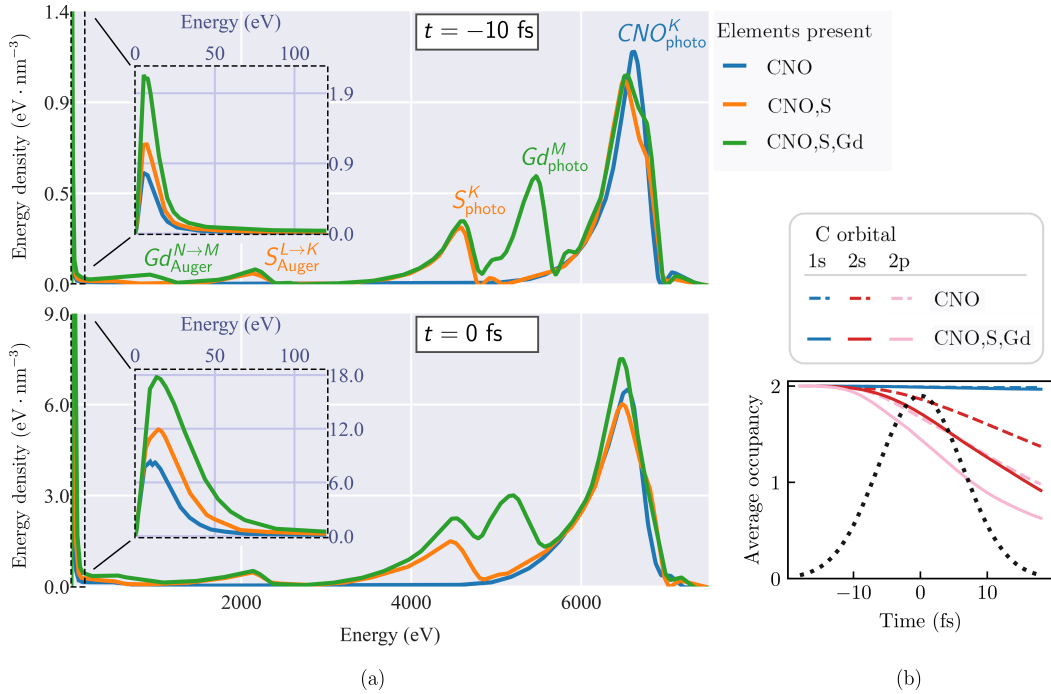


FIG. 3. (a) Snapshots of the free electron energy distribution for the light-atom control (blue), lysozyme (orange), and lysozyme.Gd (green). Inset plots show the distributions at the scale of the thermalized electrons. Snapshot times are denoted relative to the pulse's peak intensity ($t = 0$ fs). (b) Corresponding evolution of the average occupancy of the electron orbitals of carbon in the light-atom control (broken lines) and lysozyme.Gd (solid lines); the black dotted line traces the temporal pulse profile. The modeled 15 fs FWHM Gaussian pulse's fluence was $1.75 \times 10^{12} 7.112 \text{ keV ph}\cdot\mu\text{m}^{-2}$.

As is standard for studies of radiation damage [2, 29, 30, 32], this work employs an R factor as a metric for the severity of the radiation damage – specifically, the weighted mean error between the ideal and damaged scattering patterns R_{dmg} . While directly comparing this measure with experimental R factors would be misleading, it may be reasonably used to predict the relative contribution of damage to experimentally analogous noise in initially identical structures (a constrained usage compared to prior works, see Appendix B). The presence of gadolinium and sulfur increases R_{dmg} by 59% (relative to the light atom control), indicating their contributions to damage-induced noise are substantial.

Simulations performed with **RADDOSSE-XFEL**, a Monte Carlo code that does not include high-density effects like TBR or the depletion of the ionic states, also predicted a strong impact by gadolinium and sulfur on the light atoms' ionization. These simulations demonstrated that excluding later ionization is key to the effect: calculating the absorbed doses with **RADDOSSE-3D**, which assumes EII to be instantaneous, grossly underestimated the relative contribution of heavy atoms.

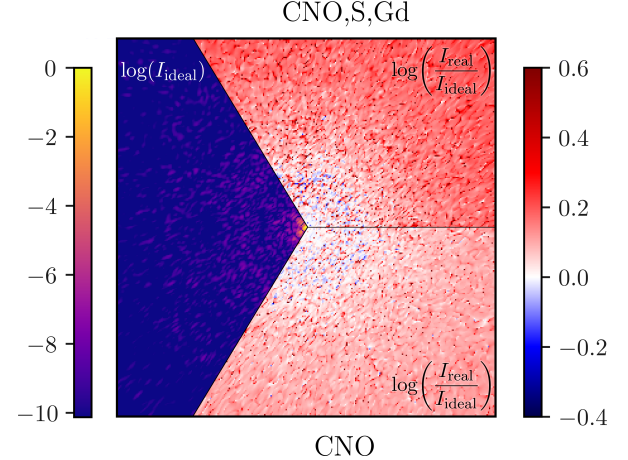


FIG. 4. Effect of damage on the scattering pattern of the lysozyme protein with (upper-right) and without (lower-right) heavy element ionization. The left sector shows the log of the ideal (noise-free) scattering pattern. Sectors on the right plot the log of the ratio of the damage-affected and ideal scattered irradiances, each normalized to have unit intensity at the center [30]. The structure of the lysozyme protein includes its full eightfold symmetry (which is broken by the stochastic electronic damage) and only includes the light atoms' elastic scattering contributions. The resolution at the edge is 2 Å. Each simulation modeled a 15 fs FWHM Gaussian pulse with a fluence of $1.75 \times 10^{12} 7.112 \text{ keV ph}\cdot\mu\text{m}^{-2}$.

A. Comparing the ionization behavior of light and heavy elements

The primary electron production rate rises substantially with higher Z . This is partly due to the Z^4 scaling of the photoabsorption cross-section. It also results from the fall in decay transition lifetimes – from 10 fs in carbon to near or below 1 fs for elements heavier than sulfur [19, 71] – which both mitigates frustrated absorption resulting from core holes [72] and shortens the delay between photoionization and Auger electron emission. This suggests that on short timescales, the influence of heavy atoms on electronic damage is mainly distinguished by their primary ionization behavior. It can be seen how this could make heavy elements significant sources of damage by picturing a heavy atom within a mass of light atoms exposed to an XFEL pulse. The heavy atom undergoes rapid primary ionization at early times, seeding many electron cascades that each impact and ionize many light atoms over 3–20 fs [3].

To verify this picture, AC4DC was used to simulate the electron dynamics of a homogeneous ‘Fe-doped’ target containing 1 Fe^{2+} ion for every 99 light atoms under four models:

- a) Primary ionization only.
- b) All ionization in CNO only.
- c) All ionization in CNO and primary ionization in Fe.
- d) All ionization processes.

The time-dependent ionic states of these systems under a 15 fs pulse with a square temporal profile are visualized in Fig. 5. The pulse was simulated at a fluence on the upper end of modern capabilities (10^{13} 10 keV $\text{ph}\cdot\mu\text{m}^{-2}$), where the influence of secondary ionization is comparatively weak. Contrasting models a) and b) with the complete dynamics of model d), it is clear that both light-atom secondary ionization and the presence of the Fe ions are essential parts of the dynamics. The similarity of models c) and d) shows that the influence of the Fe ions almost entirely originates with their primary ionization processes.

The rapid ejection of electrons from the K-shells of Fe ions is sustained by the electrons in higher orbitals, which fill core holes on a subfemtosecond timescale through Auger decay and, to a lesser extent, fluorescence. As a result, the 1s orbital remains almost full until the higher shells are stripped. This Auger cycling (a mechanism previously identified by Refs. [52] and [73]) implies the early-time photoionization rate of the Fe ions scales almost linearly with photon intensity.

From this perspective, it can be understood why the heavy elements in lysozyme and lysozyme.Gd have a disproportionate influence on electronic damage. Although

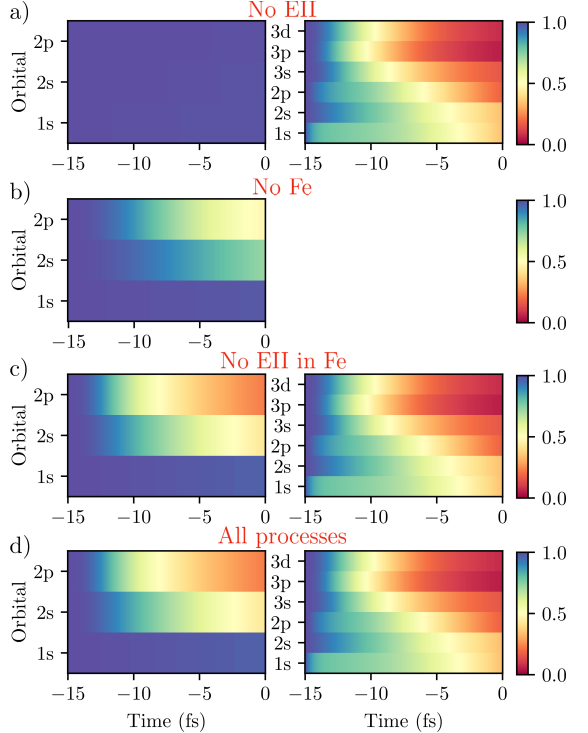


FIG. 5. Impact of various approximations to the simulation on the evolution of the Fe-doped target’s C (left) and Fe (right) orbital occupancies, under a 15 fs square pulse containing 10^{13} 10 keV $\text{ph}\cdot\mu\text{m}^{-2}$. All densities are normalized to 1 in the fully occupied state. In row (a), EII is switched off for all atoms, while in (c), only EII in the heavy atoms is ignored. (b) displays the evolution of the carbon atoms where the Fe ions are replaced with nitrogen, representing a light atom model. In (d), all ionizing processes are accounted for. TBR was disabled in these simulations to make computation of row (d) feasible. While accounting for both heavy elements and light atoms’ secondary ionization is critical to accurately predicting the depletion of electrons in the light ions, ignoring secondary ionization in the heavy atoms has little effect.

the electrons ejected from light atoms make up the overwhelming majority of the free electron population, most of these electrons are ejected by EII cascades, of which a substantial fraction are seeded by the primary ionization of S and Gd atoms (see Fig. 6). The amount of damage caused by a cascade will depend on the energy of the instigating primary electron, so the order 1 keV separations between the CNO, S, and Gd photoelectron and Auger emission energies observable in Fig. 3(a) lead to further differences in how they affect the target’s secondary ionization. See Sec. IV A for further details. It should be noted that in the lysozyme.Gd simulation, the ionizable shells of Gd (M, N, and O) were almost completely stripped of electrons by $t = 0$; in reality, the highly charged Gd ions would be replenished by bound electrons transported from neighbouring atoms [73], likely leading to a stronger damage seeding effect.

Finally, we remark on the importance of the pulse profile on these dynamics. Previous works have gen-

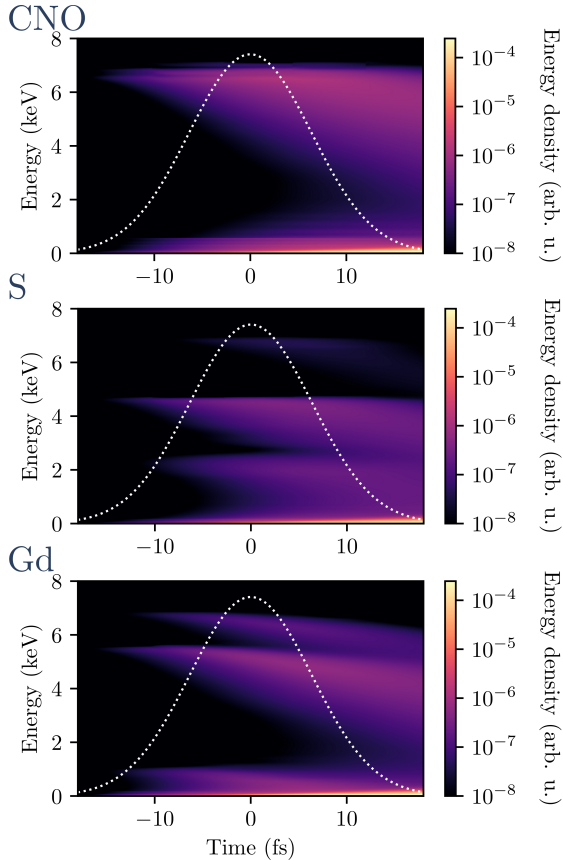


FIG. 6. Contributions of each element to the free electron cascades in lysozyme.Gd. Each continuum shows the evolution of the electrons freed from EII cascades seeded by the atoms denoted in the upper-left corner, including the primary electrons. The target was simulated under a 15 fs FWHM Gaussian pulse with a fluence of $1.75 \times 10^{12} 7.112 \text{ keV ph}\cdot\mu\text{m}^{-2}$

erally modeled the temporal intensity profile as either square [34, 57] or Gaussian [57, 58]. The ionization dynamics proved to be sensitive to this choice (see Fig. S1). Repeating the lysozyme.Gd simulation (Fig. 3) with a square pulse of the same fluence, energy, and FWHM showed R_{dmg} to be 30% higher in the Gaussian case. This can be attributed to the outsized effect of earlier EII cascades [74], induced by the leading tail of the pulse. Such cascades have a long period to ionize the target before the bulk of the elastic X-ray scattering.

IV. DAMAGE BY DIFFERENT TRACE ELEMENTS

In this section, we present the results of simulations designed to examine how the energy-level structure of a trace, heavy element in a biological target affects electronic damage. Ionization dynamics were modeled in

targets with the atomic ratio of non-derivative lysozyme, but with sulfur (1% of the atoms) replaced by ‘dopant’ atoms of some element. The ‘N-doped’ and ‘S-doped’ targets considered in this section thus correspond, respectively, to the light-atom control and non-derivative lysozyme targets considered in Sec. III.

The total number of modeled atomic configurations scales like the factorial of the total number of subshells of an element’s ground state, making heavier elements very costly to simulate. For computational expedience, $n \geq 2$ shells of $Z \geq 30$ elements were modeled with a single angular momentum (i.e. a single energy level). Benchmarks showed this approximation had negligible consequences for the overall dynamics (see Fig. S2).

A. Photon and primary electron energy

Fig. 7(a) shows that the choice of dopant substantially impacts R_{dmg} . At all energies, R_{dmg} sees a wide range of values across the targets. Most traces show decreasing damage with increasing photon energy, consistent with prior studies [2]; however, the traces for the targets doped with Fe^{2+} ($Z=26$), Zn^{2+} ($Z=30$), and Se ($Z=34$) buck this trend, with the transition over the K-edge of the dopant roughly doubling R_{dmg} in each case. This reflects the substantial contribution of the K-shell to the primary ionization of these dopants; the 1s orbitals dominate the photoabsorption cross-sections of their atoms and are replenished on a subfemtosecond timescale by Auger cycling (see Sec. III A).

Perhaps more surprisingly, R_{dmg} continues to increase above the K-edges for ~ 2 keV despite decreases in the photoabsorption cross-section. To understand this, one can consider a free electron of energy E interacting with a gas of hydrogenic atoms, with electrons bound by energy B . As E falls, the EII cross-section grows, causing an increased ionization rate down to $E \simeq B$ [67, 75]. Fig. 8 sketches typical showers of secondary electrons from a single primary electron in the $E \gg B$ regime. It can be seen that the increase in ionization cross-section as the impacting electron’s velocity falls creates a trade-off: higher-energy cascades progress more slowly, but they have the potential to free a greater number of electrons [3]. When counting all ionization events over a fixed duration, there will be a maximally ionizing cascade energy. This implies the existence of a ‘maximally damaging’ cascade energy E_{max} , though of lower energy since the earlier ionizations of a more rapid cascade have a more significant influence on the scattering pattern (further magnified by Bragg gating [3, 76, 77]). Due to the higher photoabsorption cross-section near the edge, the most damaging photons eject primary electrons with energies below E_{max} ; however, simulations that control for the rate of primary ionization show the difference to be slight (about 0.5 keV, see Appendix C).

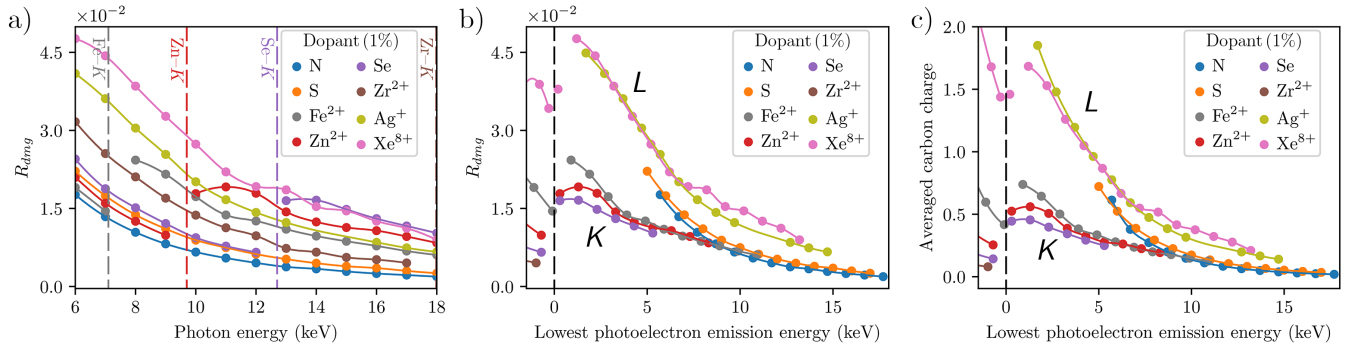


FIG. 7. Electronic damage in protein targets with different heavy element dopants. Each trace corresponds to a target modeled as lysozyme's light atom structure and doped with the corresponding atomic species in the legend (dopant:CNO = 1:99). (a) shows R_{dmg} against photon energy for each target, with dashed lines indicating dopant absorption edges. The points are shifted in (b) to align with the separation between the deepest ionizable shell (DIS) of the dopants at 18 keV, i.e. the lowest energy photoelectrons emitted by said DIS. (c) shows the pulse-integrated charge of the targets' carbon ions for comparison. The lowest photoelectron emission energy is a stronger predictor than photon energy for damage in the targets. The distinct groups formed are annotated with the DIS of the members' dopants. As elastic scattering by dopants is ignored, R_{dmg} is a function of the light atom electronic states. The interpolating lines are included as a guide for the eye. Each simulation used a 15 fs FWHM Gaussian pulse with 10^{12} ph· μm^{-2} fluence.

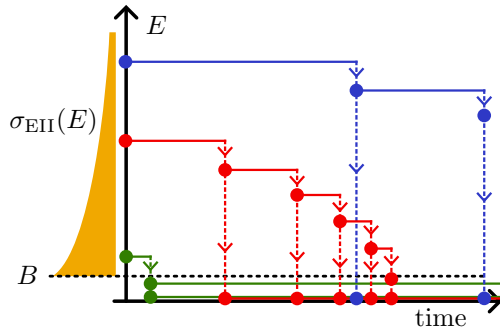


FIG. 8. The fate of energetic free electrons incident on a gas of bound electrons; binding energy B . Each branching event represents the most likely electron-electron scattering process: an electron of energy E 'only just' ionizes an atom, leaving one electron at zero energy and another at $E - B$. Intermediate-energy electrons (red) undergo the most impact ionization events in a fixed timeframe.

When plotted against the lowest photoelectron energy (LPE) at emission instead of the photon energy, the traces form two distinct groups: the 'K-group', targets doped by an element whose 'deepest ionizable shell' (DIS) in the considered energy range is the K-shell (N, S, Fe, Zn, Se), and the 'L-group', where it is the L-shell (Ag, Xe). The average ionization of carbon atoms in the sample follows a similar trend (Fig. 7(c)). The split in groups again appears to be a result of Auger cycling. As all heavy dopants' DIS are maintained near maximum occupancy by decay processes, the production rate of ionizing electrons by Ag^+ and Xe^{8+} is scaled by a factor of ~ 4 relative to the other dopants at an equivalent LPE, due to the higher electron capacity of their L-shells.

In general, the variation in electronic damage across the targets with respect to photon frequency is predominantly controlled by the LPE of the dopants and the shell number of the DIS. However, the traces of the N, S, and Fe-doped targets deviate from the main K-group in Fig. 7(b) and (c) for photon energies at or below 8 keV. In these cases, the photoelectrons ejected from the light atoms are of a low enough energy to contribute significantly to their secondary ionization (relative to the dopants). Since the Zn and Se K-edges are above 8 keV, their traces show no deviation. It is unsurprising that the L-group does not contain such outliers, as the primary electron contribution of the L-group dopants is much more dominant.

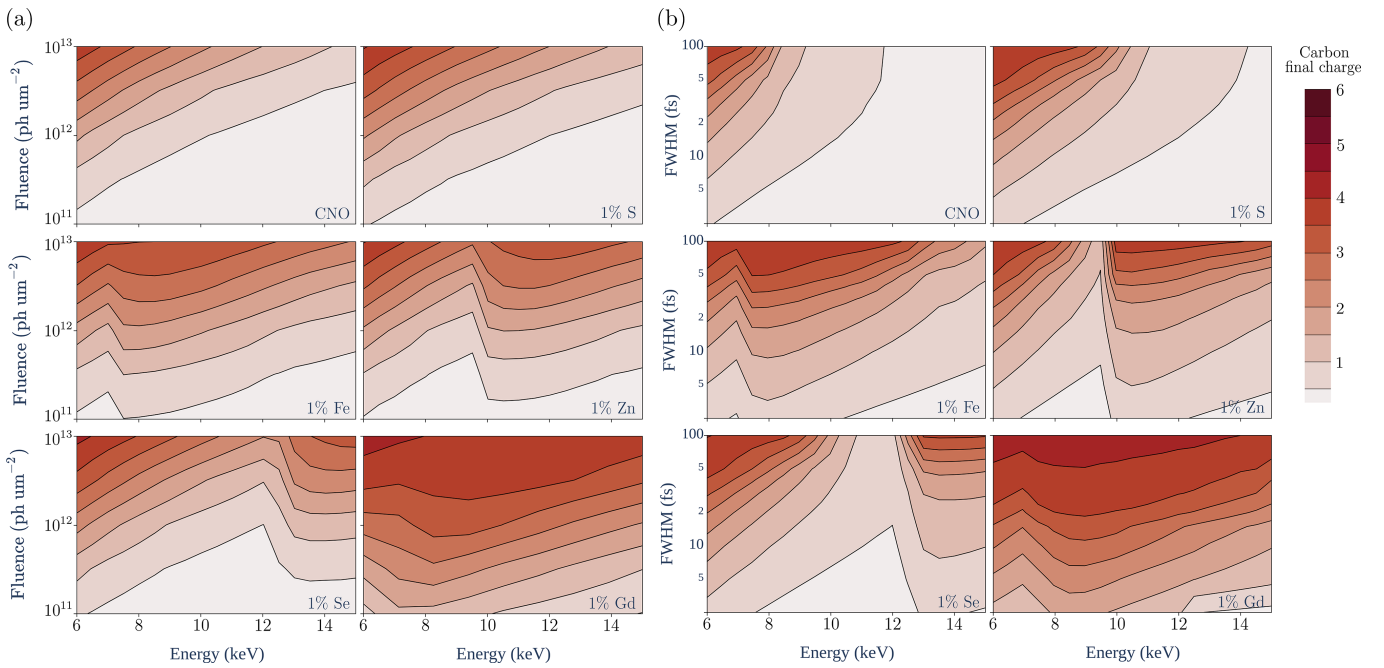


FIG. 9. Effect of chemical composition on the electronic damage landscape. (a) Damage landscape for 15 fs FWHM Gaussian pulses. (b) Damage landscape for Gaussian pulses of 10^{12} $\text{ph}\cdot\mu\text{m}^{-2}$ fluence. Each plot maps the average charge of carbons at the end of the illumination ($+1.2$ FWHM) of a mock derivative of lysozyme, where sulfur is substituted for the element denoted in the lower-right corner ('CNO' denotes the light-atom control, where N is the substitute). Each plot uses (a) 133 or (b) 190 data points. The sharp features in the plots for targets doped by heavier elements correspond to the dopant absorption edges.

B. Damage landscape

Repeating the simulations shown in Fig. 7 while ignoring heavy-atom secondary ionization had little effect on the traces, as predicted by the analysis in Sec. III A. Since this substantially reduces the number of configurations to be processed in the EII and TBR calculations, additional simulations were performed using this approximation to map the landscape of damage [2] for each target (Fig. 9).

Contour plots of the charge accumulated by the carbon atoms, as functions of photon energy and fluence, (Fig. 9(a)) or pulse width (Fig. 9(b)), show broad and significant differences due to the dopants. The effect of sulfur on the dynamics is relatively consistent; across the parameter space of Fig. 9, the S-doped target experiences levels of ionization that the pure CNO target only sees at 20–40% higher intensities. The impact of the heavier dopants is more variable due to their deep absorption edges, which are distinctly visible in these plots – the most extreme case is the Se-doped target, where the elevation in damage from increasing the photon energy from 12.5 keV to 13.5 keV is similar to the elevation in damage from increasing the pulse's fluence by a factor of 3–4 (Fig. 9(a)), or from increasing the pulse's duration by an order of magnitude (Fig. 9(b)).

Inspection of Fig. 9 shows that the ionization in the doped targets consistently sees a local maximum around

a LPE of 2 keV, suggesting this may serve as an approximate value for E_{max} in this regime (see Sec. IV A). Both the slow Auger electrons and fast photoelectrons ejected by light atoms are well away from this value for E_{max} in typical hard X-ray SFX experiments, while the primary electrons ejected by heavy atoms are almost always closer. This is the case in the lysozyme.Gd scenario considered in Sec. III. As annotated in Fig. 3(a), the photoelectrons ejected by the heavy elements are closer to 2 keV than those of the light atoms and thus more damaging, and the same is true of the Auger electrons. The tendency of heavy atoms to eject electrons with 'intermediate' energies closer to E_{max} thus contributes to the strength of their effect.

V. INTERSTITIAL SOLVENT

The presence of aqueous solution in targets is ubiquitous to protein SFX, encapsulating the structure and making up a substantial volume of the protein crystal [24, 53, 78]. Prior work has shown that atoms within a neutral, light-atom target will be affected by high-energy EII cascades initiated >100 nm away [3, 29]. This makes cascades instigated within the solvent a significant source of electronic damage. It becomes especially important to consider the composition of the solvent where heavy elements have a significant effect on electronic damage, as

the concentrations and species of heavy elements will often be quite different between solution and protein.

In Sec. III, lysozyme.Gd was modeled as a continuous target using the density and chemical composition of only the protein. We now revisit this scenario, but model a solvated crystal using the density and chemical composition of the full unit cell of real lysozyme.Gd crystals. Approximately half of the volume is taken up by water molecules (oxygen), mixed with Gd in approximately equal concentration as in the protein [69]. We neglect the presence of any salts. Treating the electronic damage dynamics of the target as homogeneous requires the following three idealizations in place of the assumption of a continuous protein material: (I) the crystal is infinite, (II) there is instantaneous mixing of free electrons with energies above 1 keV between the interstitial solvent and protein, (III) the solvent's emission of primary electrons below 1 keV (corresponding to light-atom Auger emissions) per unit volume is identical to the protein's.

The results for these simulations are shown in Table I. In each case, the damage was increased when the solvent's contribution was accounted for. This may be attributed to the light atoms' higher primary electron emission rate in the solvated target, due to oxygen making up the majority of the light atoms rather than more weakly absorbing carbon. Unsurprisingly, the effect of introducing Gd to both targets in equal concentrations leads to a relatively similar effect on R_{dmg} , while sulfur's effect is much smaller due to its reduced concentration.

The dynamics in the single particle imaging limit were also considered by modeling a target as an isolated lysozyme protein suspended within an infinite mother liquor drop. In this regime, the solution makes up essentially the entirety of the protein's environment within the 100 nm scale spanned by the high-energy electron cascades. The high-energy cascades seeded by the protein should largely dissipate in the mother liquor, while in turn the mother liquor's electron emissions will dominate the ionization of the protein. It is thus assumed that high-energy electrons seeded by the protein can be neglected entirely. Thus for certain targets, the ionization suffered by the protein may be modeled by considering only the solvent, which has a similar atomic density. Lysozyme.Gd suspended in pure water was not considered a viable model under this approximation, as gadolinium ions eject Auger electrons with energies on the order of 1 keV that cannot be assumed to instigate cascades well above lysozyme's 10 nm length scale [29].

VI. DISCUSSION

While it is well understood that the width of an XFEL pulse significantly affects the dose absorbed by a target (during exposure) and thus the maximum tolerable fluence [2, 3, 29, 36, 79], the results presented here suggest

R_{dmg} , Continuous protein (100% protein)			
Protein	Light	Lysozyme	Lysozyme.Gd
7.1 keV	0.0177	0.0226	0.0274
9.0 keV	0.0113	0.0150	0.0306
R_{dmg} , Solvated crystal (50% protein, 50% solvent)			
Solvent	Water		10 mM Gd
Protein	Light	Lysozyme	Lysozyme.Gd
7.1 keV	0.0250	0.0266	0.0294
9.0 keV	0.0163	0.0180	0.0275
R_{dmg} , Single particle			
Solvent	Water		10 mM Gd
Protein	Light	Lysozyme	Lysozyme.Gd
7.1 keV	0.0309	0.0309	—
9.0 keV	0.0212	0.0212	—

TABLE I. Comparison of the frequency dependence of R_{dmg} under various models of the target's large-scale structure and composition. The “light” protein is the light-atom control – lysozyme with S substituted for N. Concentrations of protein and solvent are given in % (v/v). The continuous protein structure corresponds to the model considered in Sec. III. Missing values in the single particle simulations correspond to scenarios where approximating the target as homogeneous cannot be justified. Each simulation modeled a Gaussian 15 fs FWHM pulse with a fluence of $1.75 \times 10^{12} 7.112 \text{ keV ph}\cdot\mu\text{m}^{-2}$.

the absorbed dose can also be significantly affected by the presence of heavy atoms and the energy of their primary electron emissions. For all targets considered, a high-energy regime exists in which the general principle that ‘higher photon energy = less damage’ remains true. However, for certain targets, the maximum photon energies available from XFEL sources are too low to enter this regime (Fig. 9). This is a departure from conventional crystallography, where higher energies are broadly beneficial. More positively, this suggests SFX experiments may be able to control the severity of damage through the choice of X-ray frequency or solvent composition. For example, excluding gadolinium from just the interstitial solvent of the lysozyme.Gd crystal reduced R_{dmg} by 19% for the 9 keV beam (Table I).

Elements much heavier than sulfur, such as Se and Gd, are often introduced to targets for anomalous phasing, generally in tandem with an X-ray energy just above their ionization edges [41, 42, 44, 47]. It is commonly held that difficulties in applying the technique to SFX can be mitigated by using increased heavy atom concentrations [41, 42], but the results of the present work suggest this is a trade-off in the ultrafast regime, boosting the anomalous signal at the cost of additional damage to the light atom structure. For example, Fig. 9(b) shows pulses as long as 100 fs are predicted to cause less electronic damage to regular lysozyme than a 5 fs pulse of the same fluence would to lysozyme where methionine is substituted for selenomethionine. This cost is reduced when phasing is performed with an X-ray frequency well above the absorption edge, as has been done in native phasing experiments [37, 48].

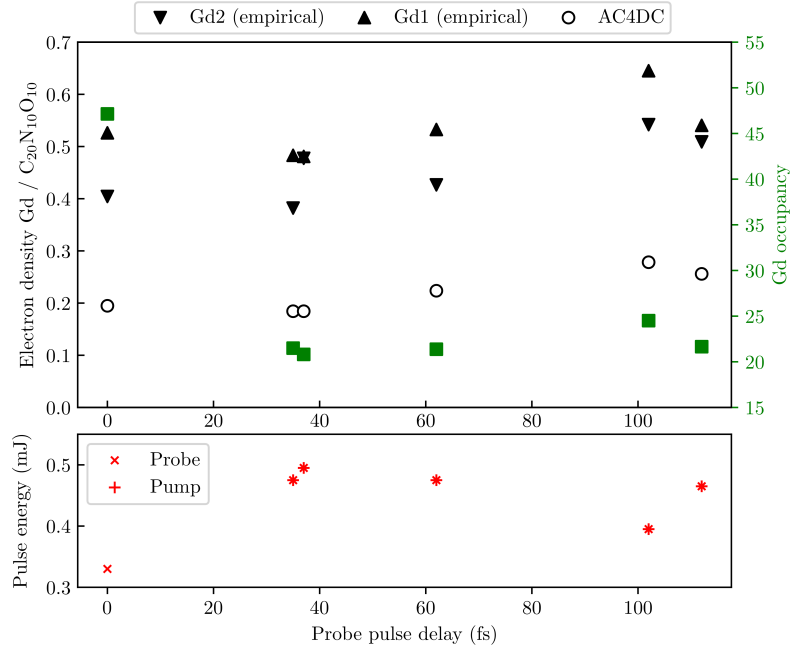


FIG. 10. Electron density ratio of Gd ions to light ions (EDR) in lysozyme.Gd as observed in experiments by Ref. [27] and in corresponding AC4DC simulations. The pulse energy corresponds to individual pump or probe pulses. All data points correspond to a pump pulse at $t = 0$ fs and a probe pulse at some delay, except for the ‘single pulse’ at the $t = 0$ fs data point. The simulated EDR was computed from the probe-intensity-averaged occupancy of a Gd ion over the occupancy of a reference region ($C_{20}N_{10}O_{10}$, as in Ref. [27]). The square points correspond to the probe-intensity-averaged occupancy in simulations. The EDR of the simulations is about half the average value observed empirically, likely due to the simulation neglecting the transport of bound electrons to the highly charged Gd ions. The relative changes in the empirical EDR between probe pulse delays are remarkably similar to those predicted by AC4DC. It can be seen that EDR is not commensurate with the occupancy of Gd in the simulations. Secondary ionization of Gd ions was not modeled.

There is preliminary evidence that these considerations are relevant in practice. Nass *et al.* attributed unusual noise in the scattering profile of lysozyme.Gd to increased radiation damage induced by Gd [27]. Our modeling supports this inference, as it found the addition of just Gd to the target (alongside C, N, O and S) increases the pump-pulse R_{dmg} by 17–21% (see Table I). However, Fig. 9(a) suggests that, at the fluence of this experiment (nominally $3.5 \times 10^{12} \text{ ph} \cdot \mu\text{m}^{-2}$, though likely lower in reality [27, 80]), the 7.1 keV photon energy used (just low enough to avoid ionizing the L_3 -edge of the Gd ions) would be close to the optimal choice for minimizing damage in this case. Indeed, while increasing the photon energy to 9 keV caused R_{dmg} to fall by 32–34% for the scattering pattern of lysozyme, it *rose* by 9–11% for lysozyme.Gd.

The ionization of Gd ions in lysozyme.Gd under XFEL pulses has previously been investigated by Refs. [27] and [47]. The charge density of the Gd ions is inferred from the integrated electron density around the Gd site relative to a reference region of light atoms, which we refer to as the electron density ratio (EDR). Notably, this measure indicated the ionization of Gd to be unexpectedly low in both studies. Fig. 10 compares EDR values obtained from pump-probe experiments by Ref. [27] (us-

ing a light atom reference region, $C_{20}N_{10}O_{10}$) with predictions from simulations of these experiments by AC4DC using the solvated lysozyme.Gd target. The simulated EDRs accurately reproduce the features of the experimental data, but rescaled by a factor of 2. This systematic offset may be due to AC4DC neglecting bound-to-bound electron transport – as alluded to in Sec. III A, this was previously shown to slow the charge gain of iodine in iodobenzene [73], which contains fewer light atoms than the Gd complex. For the four EDR values where the total pulse energy has a range of 0.95–0.99 mJ (35 fs, 37 fs, 62 fs, and 112 fs), the EDR rises with increasing probe delay. We argue this is consistent with the picture of the dynamics described in Sec. III A, which highlights that secondary ionization events – the only processes active during the dead time between pump and probe – affect the light atom dynamics far more strongly than the heavy atom dynamics. This implies that the EDR does not gauge the electron density of the heavy atoms but instead serves as a rough indicator of the ratio of secondary ionization to primary ionization. Under this perspective, the EDRs at 0 fs and 102 fs – which correspond to lower pulse energies – are raised due to the greater significance of secondary ionization at lower fluences.

Using a similar methodology to Ref. [27], Ref. [47] also

attempted to measure the charge of Gd in two cases – ‘high fluence’ and ‘low fluence’, peaking at 7.8 and $0.13 \times 10^{12} \text{ ph}\cdot\mu\text{m}^{-2}$ respectively. The work reports only the difference in pulse-averaged Gd charge between these cases, termed the ‘charge contrast’, as measured by computing the EDR and assuming negligible light-atom ionization. A charge contrast of 8.8–12 electrons per Gd was observed; however, theoretical modeling using the **XATOM** toolkit predicted that the Gd charge difference ought to be 25. We repeated this modeling using **AC4DC**, finding an even more extreme 33.1. The apparent discrepancy between theory and experiment can be largely attributed to light atom ionization reducing the denominator of the EDR (see Fig. S4) – we obtain a charge contrast of 18.2 after making this correction. When performing this calculation, it was crucial to properly account for the cascade seeded by the Gd ions – modeling that ignored Gd ion contributions to the free electron distribution saw a value of 21.5 with this method.

VII. CONCLUSIONS

The zero-dimensional non-LTE model employed in this study suggests that a significant amount of damage to biological macromolecules under XFEL illumination is seeded by heavy atoms, with even the presence of native sulfur atoms significantly affecting the damage-induced loss of coherence in the scattered wavefield. This result might appear surprising given such targets only contain heavy elements in trace quantities; however, closer inspection shows this outcome to reasonably follow from two key points: (I) Heavier species emit photo- and Auger electrons at much higher rates, considerably boosting the number of secondary ionization cascades instigated within the light atom bulk. (II) Relative to the 10 fs timescale on which the structural signal is captured, light-atom-sourced electron avalanches will either have a very low energy and thus dissipate prematurely, or have a very high energy and thus a small EII rate; in contrast, avalanches initiated by heavy atoms, with energies between these two extremes, more severely degrade the captured structural signal. The non-LTE treatment of the electron continuum was necessary to capture this latter point.

The addition of heavy atoms to the environment of proteins – such as potassium and sodium ions in the mother liquor – is routine in protein crystallography; however, the results of this work suggest that in the XFEL regime their use becomes a trade-off for additional damage. Judicious choices to reduce the number of low-intermediate energy primary electron emissions may thus improve experimental outcomes where damage is a concern, or where controlling for damage across pulse parameters is necessary. Specific to *de novo* refinement, anomalous phasing methodologies that allow for weaker anomalous signals would see a reduction in

damage-induced noise, suggesting a strength for native phasing over artificial introduction of heavier elements such as Gd. Further, the production of primary electrons near the maximally ionizing energy can be avoided entirely with careful choice of photon frequency.

The nonlinear dynamics highlighted in this study suggest two areas for future models to incorporate. (I) The dependence of the damage on the temporal pulse profile indicates a necessity for modeling of the dynamics under more realistic SASE pulse profile statistics, for which there exist a number of contemporary approaches [81–83]. (II) The effect of heavy atoms suggests a significance to the mother liquor’s composition in conjunction with electron transfer across the crystal boundary and the interstitial solvent. It is likely, for example, that the mother liquor’s high-energy electrons replace those of the crystal to an extent dependent on the crystal’s size.

The obvious limitation of the presented model is its zero-dimensional treatment. Target substructures such as metal cofactors often have order 10 nm separations, and the large-scale distribution of heavy atoms is generally non-uniform due to the differing compositions of the protein and its aqueous environment. Naively, this suggests heavy atoms produce a ‘sphere’ of electronic damage in their local region, with the distance spanned dependent on photon energy. However, whether such heterogeneous correlations actually occur is complicated by the non-uniformity in the large-scale solvent-protein structure of real targets. A model fit for exploring this possibility will likely need to break the crystal symmetry and account for spatial variation in electron density on the global scale of the target.

For the most part, this work has restricted analysis to targets where heavy elements make up 1% of the atomic population, but this is far from sufficient to generalize the influence of heavy atoms across the varied ratios seen in real targets, including targets containing multiple heavy elements. However, it is evident that experimental differences generally considered marginal in traditional crystallography can substantially affect the amount of radiation damage suffered by targets in the ultrafast regime. This complexity emphasizes the value of using theoretical modeling to inform SFX experimental design – a role it is already fulfilling [36] – particularly as a tool for gauging the viability of successful refinement in the high-intensity regime. The zero-dimensional framework employed in **AC4DC** can capably examine the complete electronic damage dynamics across a large number of candidate pulse parameterizations without significant investment of computational resources. For studies concerned with the ions’ motions, the simulation may be integrated within a hybrid plasma-MD framework [33, 56], where delegation of the ultrafast electron dynamics to a zero-dimensional model makes simulating the molecular dynamics of 10–100 nm scale structures feasible.

ACKNOWLEDGEMENTS

We thank A/Prof. Nadia Zatsepin, Swinburne University of Technology, Hawthorn, Australia, for feedback on the paper's discussions of SFX experimental methods and Thippayawis Cheunchitra, University of Melbourne, Parkville, Australia, for inspiring examination of the influence of absorption edges on the damage landscape.

[1] B. Sabine and F. Petra, Review of serial femtosecond crystallography including the covid-19 pandemic impact and future outlook, *Structure* **31**, 1306 (2023).

[2] R. Neutze *et al.*, Potential for biomolecular imaging with femtosecond x-ray pulses, *Nature* **406**, 752 (2000).

[3] H. N. Chapman, C. Caleman, and N. Timneanu, Diffraction before destruction, *Philos. Trans. R. Soc. B* **369**, 20130313 (2014).

[4] M. Suga *et al.*, Native structure of photosystem ii at 1.95 Å resolution viewed by femtosecond x-ray pulses, *Nature* **517**, 99 (2015).

[5] J. Tenboer *et al.*, Time-resolved serial crystallography captures high-resolution intermediates of photoactive yellow protein, *Science* **346**, 1242 (2014).

[6] S. Pandey *et al.*, Time-resolved serial femtosecond crystallography at the European XFEL, *Nat. Methods* **17**, 73 (2020).

[7] M. Suga *et al.*, Time-resolved studies of metalloproteins using X-ray free electron laser radiation at SACLAA, *Biochim. Biophys. Acta - Gen. Subj. Novel Measurement Techniques for Visualizing 'live' Protein Molecules*, **1864**, 129466 (2020).

[8] P. Kanupriya *et al.*, Femtosecond structural dynamics drives the trans/cis isomerization in photoactive yellow protein, *Science* **352**, 725–729 (2016).

[9] J. Standfuss, Membrane protein dynamics studied by x-ray lasers – or why only time will tell, *Curr. Opin. Struct. Biol.* **57**, 63 (2019).

[10] C. Melissa, P. Suraj, S. Juan, *et al.*, High-resolution crystal structures of transient intermediates in the phytochrome photocycle, *Structure* **29**, 743 (2021).

[11] M. Suga *et al.*, Light-induced structural changes and the site of o=o bond formation in psii caught by xfel, *Nature* **543**, 131 (2017).

[12] M. Dasgupta *et al.*, Mix-and-inject XFEL crystallography reveals gated conformational dynamics during enzyme catalysis, *Proc. Natl. Acad. Sci. U. S. A.* **116**, 25634 (2019).

[13] O. Jose, L. *et al.*, Enzyme intermediates captured “on the fly” by mix-and-inject serial crystallography, *BMC Biol.* **16**, 59 (2018).

[14] J. A. Hull *et al.*, XFEL structure of carbonic anhydrase II: a comparative study of XFEL, NMR, X-ray and neutron structures, *Acta Crystallogr. D* **80**, 194 (2024).

[15] J. C. H. Spence, Outrunning damage: Electrons vs X-rays-timescales and mechanisms, *Struct. Dyn.* **4**, 044027 (2017).

[16] M. M. Seibert *et al.*, Single mimivirus particles intercepted and imaged with an X-ray laser, *Nature* **470**, 78 (2011).

[17] S. Boutet *et al.*, High-Resolution Protein Structure Determination by Serial Femtosecond Crystallography, *Science* **337**, 362 (2012).

[18] H. N. Chapman, Structure Determination Using X-Ray Free-Electron Laser Pulses, in *PROTEIN CRYSTALLOGRAPHY: Methods and Protocols*, Vol. 1606, edited by A. Wlodawer, Z. Dauter, and M. Jaskolski (Humana Press Inc, 2017) pp. 295–324.

[19] K. Nass, Radiation damage in protein crystallography at X-ray free-electron lasers, *Acta Crystallogr. D* **75**, 211 (2019).

[20] H. N. Chapman *et al.*, Femtosecond X-ray protein nanocrystallography, *Nature* **470**, 73 (2011).

[21] C. Gisriel *et al.*, Membrane protein megahertz crystallography at the european xfel, *Nat. Commun.* **10**, 5021 (2019).

[22] M. S. Hunter and P. Fromme, Toward structure determination using membrane–protein nanocrystals and microcrystals, *Methods* **55**, 387 (2011), membrane Protein Technologies for Structural Biology.

[23] J. Martin and A. Sawyer, Elucidating the structure of membrane proteins, *BioTechniques* **66**, 167 (2019).

[24] F.-Z. Zhao *et al.*, A guide to sample delivery systems for serial crystallography, *FEBS J.* **286**, 4402 (2019).

[25] M. Schmidt, Mix and inject: Reaction initiation by diffusion for time-resolved macromolecular crystallography, *Adv. Condens. Matter Phys.* **2013**, 167276 (2013).

[26] A. V. Martin and H. M. Quiney, Coherence loss by sample dynamics and heterogeneity in x-ray laser diffraction, *J. Phys. B-At. Mol. Opt. Phys.* **49**, 244001 (2016).

[27] K. Nass *et al.*, Structural dynamics in proteins induced by and probed with X-ray free-electron laser pulses, *Nat. Commun.* **11** (2020).

[28] B. Abbey *et al.*, X-ray laser-induced electron dynamics observed by femtosecond diffraction from nanocrystals of Buckminsterfullerene, *Sci. Adv.* **2**, 2375 (2016).

[29] C. Caleman *et al.*, On the feasibility of nanocrystal imaging using intense and ultrashort x-ray pulses, *ACS Nano* **5**, 139 (2011).

[30] H. M. Quiney and K. A. Nugent, Biomolecular imaging and electronic damage using X-ray free-electron lasers, *Nat. Phys.* **7**, 142 (2011).

[31] A. Kozlov *et al.*, Recovery of undamaged electron-density maps in the presence of damage-induced partial coherence in single-particle imaging, *IUCrJ* **7**, 1114 (2020).

[32] M. M. Abdullah, S.-K. Son, Z. Jurek, and R. Santra, Towards the theoretical limitations of X-ray nanocrystallography at high intensity: The validity of the effective-form-factor description, *IUCrJ* **5**, 699 (2018).

[33] A. Kozlov, A. Martin, and H. Quiney, Hybrid plasma/molecular-dynamics approach for efficient xfel radiation damage simulations, *Crystals* **10**, 478 (2020).

[34] S. Hau-Riege, Nonequilibrium electron dynamics in materials driven by high-intensity x-ray pulses, *Phys. Rev. E* **87**, 053102 (2013).

[35] E. de la Mora *et al.*, Radiation damage and dose limits in serial synchrotron crystallography at cryo- and room temperatures, *Proc. Natl. Acad. Sci. U.S.A.* **117**, 4142 (2020).

[36] J. L. Dickerson, P. T. N. McCubbin, and E. F. Garman, *RADDOSE-XFEL*: femtosecond time-resolved dose estimates for macromolecular X-ray free-electron laser experiments, *J. Appl. Crystallogr.* **53**, 549 (2020).

[37] T. Nakane *et al.*, Native sulfur/chlorine sad phasing for serial femtosecond crystallography., *Acta Crystallogr. D* **71**, 2519 (2015).

[38] T. R. M. Barends *et al.*, Anomalous signal from S atoms in protein crystallographic data from an X-ray free-electron laser, *Acta Crystallogr. D* **69**, 838 (2013).

[39] K. Nass *et al.*, Pink-beam serial femtosecond crystallography for accurate structure-factor determination at an X-ray free-electron laser, *IUCrJ* **8**, 905 (2021).

[40] T. R. M. Barends *et al.*, De novo protein crystal structure determination from x-ray free-electron laser data, *Nature* **505**, 244 (2014).

[41] M. Hunter *et al.*, Selenium single-wavelength anomalous diffraction de novo phasing using an x-ray-free electron laser, *Nat. Commun.* **7**, 13388 (2016).

[42] A. Gorel, K. Motomura, H. Fukuzawa, *et al.*, Multi-wavelength anomalous diffraction de novo phasing using a two-colour x-ray free-electron laser with wide tunability, *Nat. Commun.* **8**, 1170 (2017).

[43] S.-K. Son *et al.*, Multiwavelength anomalous diffraction at high x-ray intensity, *Phys. Rev. Lett.* **107**, 218102 (2011).

[44] S.-K. Son, H. N. Chapman, and R. Santra, Determination of multiwavelength anomalous diffraction coefficients at high x-ray intensity, *J. Phys. B: At. Mol. Opt. Phys.* **46**, 164015 (2013).

[45] S. P. Hau-Riege and B. J. Bennion, Reproducible radiation-damage processes in proteins irradiated by intense x-ray pulses, *Phys. Rev. E* **91**, 022705 (2015).

[46] L. Galli, S.-K. Son, T. A. White, R. Santra, H. N. Chapman, and M. H. Nanao, Towards RIP using free-electron laser SFX data, *J. Synchrotron Radiat.* **22**, 249 (2015).

[47] L. Galli, S.-K. Son, T. R. M. Barends, *et al.*, Towards phasing using high x-ray intensity, *IUCrJ* **2**, 627 (2015).

[48] L. Galli *et al.*, Electronic damage in S atoms in a native protein crystal induced by an intense X-ray free-electron laser pulse, *Struct. Dyn.* **2**, 041703 (2015).

[49] C. Caleman *et al.*, A perspective on molecular structure and bond-breaking in radiation damage in serial femtosecond crystallography, *Crystals* **10**, 585 (2020).

[50] Z. Jurek, S.-K. Son, B. Ziaja, and R. Santra, XMDYN and XATOM: Versatile simulation tools for quantitative modeling of X-ray free-electron laser induced dynamics of matter, *J. Appl. Crystallogr.* **49**, 1048 (2016).

[51] P. J. Ho and C. Knight, Large-scale atomistic calculations of clusters in intense x-ray pulses, *J. Phys. B-At. Mol. Opt. Phys.* **50**, 104003 (2017).

[52] P. J. Ho *et al.*, The role of transient resonances for ultrafast imaging of single sucrose nanoclusters, *Nat. Commun.* **11**, 1 (2020).

[53] C. Carl *et al.*, Simulations of radiation damage in biomolecular nanocrystals induced by femtosecond x-ray pulses, *J. Mod. Opt.* **58**, 1486 (2011).

[54] A. Leonov *et al.*, Time dependence of X-ray polarizability of a crystal induced by an intense femtosecond X-ray pulse, *IUCrJ* **1**, 402 (2014).

[55] M. M. Abdullah *et al.*, Calculation of x-ray scattering patterns from nanocrystals at high x-ray intensity, *Struct. Dyn.* **3**, 054101 (2016).

[56] I. Dawod, S. Cardoch, T. André, E. De Santis, J. E, A. P. Mancuso, C. Caleman, and N. Timmeanu, Mold-Struct: Modeling the dynamics and structure of matter exposed to ultrafast x-ray lasers with hybrid collisional-radiative/molecular dynamics, *Chem. Phys.* **160**, 184112 (2024).

[57] R. Royle *et al.*, Kinetic modeling of x-ray laser-driven solid Al plasmas via particle-in-cell simulation, *Phys. Rev. E* **95**, 063203 (2017).

[58] S. Ren *et al.*, Non-thermal evolution of dense plasmas driven by intense x-ray fields, *Commun. Phys.* **6**, 99 (2023).

[59] Y.-F. Shi *et al.*, Exploring relaxation dynamics in warm dense plasmas by tailoring non-thermal electron distributions with a free electron laser, *Physics of Plasmas* **31**, 082305 (2024).

[60] H. Kitamura, Thermalization dynamics of primary and secondary electrons in metals, *J. Electron Spectros. Relat. Phenomena* **232**, 45 (2019).

[61] T. H. Kho, Relaxation of a system of charged particles, *Phys. Rev. A* **32**, 666 (1985).

[62] M. M. Abdullah, Anurag, Z. Jurek, S.-K. Son, and R. Santra, Molecular-dynamics approach for studying the nonequilibrium behavior of x-ray-heated solid-density matter, *Phys. Rev. E* **96**, 023205 (2017).

[63] A. Kozlov and H. M. Quiney, Comparison of Hartree–Fock and Hartree–Fock–Slater approximations for calculation of radiation damage dynamics of light and heavy atoms in the field of an x-ray free-electron laser, *Phys. Scr.* **94**, 075404 (2019).

[64] É. Girard *et al.*, Gadolinium derivative of tetragonal hen egg-white lysozyme at 1.7 Å resolution (2001).

[65] É. Girard, L. Chantalat, J. Vicat, and R. Kahn, Gd-HPDO3A, a complex to obtain high-phasing-power heavy-atom derivatives for SAD and MAD experiments: results with tetragonal hen egg-white lysozyme, *Acta Crystallogr. D* **58**, 1 (2002).

[66] D. Sehnal *et al.*, Mol* viewer: modern web app for 3d visualization and analysis of large biomolecular structures, *Nucleic Acids Res.* **49**, W431–W437 (2021).

[67] Y.-K. Kim and M. E. Rudd, Binary-encounter-dipole model for electron-impact ionization, *Phys. Rev. A* **50**, 3954 (1994).

[68] C. de Boor, *A Practical Guide to Splines* (Springer New York, 1978).

[69] S. Boutet *et al.*, Hen egg-white lysozyme solved from 40 fs free-electron laser pulse data (2012).

[70] I. M. Band, Y. I. Kharitonov, and M. B. Trzhaskovskaya, Photoionization cross sections and photoelectron angular distributions for x-ray line energies in the range 0.132–4.509 keV targets: $1 \leq Z \leq 100$, *At. Data Nucl. Data Tables* **23**, 443 (1979).

[71] J. Campbell and T. Papp, Widths of the atomic k -n7 levels, *At. Data Nucl. Data Tables* **77**, 1 (2001).

- [72] S.-K. Son, R. Boll, and R. Santra, Breakdown of frustrated absorption in x-ray sequential multiphoton ionization, *Phys. Rev. Res.* **2**, 023053 (2020).
- [73] A. Rudenko *et al.*, Femtosecond response of polyatomic molecules to ultra-intense hard X-rays, *Nature* **546**, 129 (2017).
- [74] H. O. Jönsson, N. Timneanu, C. Östlin, H. A. Scott, and C. Caleman, Simulations of radiation damage as a function of the temporal pulse profile in femtosecond X-ray protein crystallography, *J. Synchrotron Radiat.* **22**, 256 (2015).
- [75] T. K. Hiroya Suno, Cross section database for carbon atoms and ions: Electron-impact ionization, excitation, and charge exchange in collisions with hydrogen atoms, *At. Data Nucl. Data Tables* **92**, 407 (2006).
- [76] A. Barty, C. Caleman, A. Aquila, *et al.*, Self-terminating diffraction gates femtosecond x-ray nanocrystallography measurements, *Nature Photon.* **6**, 35–40 (2012).
- [77] C. Caleman *et al.*, Ultrafast self-gating bragg diffraction of exploding nanocrystals in an x-ray laser, *Opt. Express* **23**, 1213 (2015).
- [78] A. McPherson and A. Gavira, J., Introduction to protein crystallization, *Acta Crystallogr. F*, 2 (2014).
- [79] P. Mehrabi *et al.*, Serial femtosecond and serial synchrotron crystallography can yield data of equivalent quality: A systematic comparison, *Sci. Adv.* **7**, eabf1380 (2021).
- [80] B. Nagler, A. Aquila, S. Boutet, *et al.*, Focal spot and wavefront sensing of an x-ray free electron laser using ronchi shearing interferometry, *Sci. Rep.* **7**, 13698 (2017).
- [81] K. Dingel *et al.*, Artificial intelligence for online characterization of ultrashort X-ray free-electron laser pulses, *Sci Rep* **12**, 17809 (2022).
- [82] T. W. Guest *et al.*, A phenomenological model of the X-ray pulse statistics of a high-repetition-rate X-ray free-electron laser, *IUCrJ* **10**, 708 (2023).
- [83] E. Schneidmiller and M. Yurkov, Photon beam properties at the European XFEL (December 2010 revision) (2011).
- [84] W. L. Morgan and B. M. Penetrante, ELENDIF: A time-dependent Boltzmann solver for partially ionized plasmas, *Comput. Phys. Commun.* **58**, 127 (1990).
- [85] J. Oxenius, *Kinetic Theory of Particles and Photons: Theoretical Foundations of Non-LTE Plasma Spectroscopy*, Springer Series in Electronics and Photonics (Springer-Verlag, 1986).
- [86] S. Khurana and M. Thachuk, A numerical solution of the linear Boltzmann equation using cubic B-splines, *J. Chem. Phys* **136**, 094103 (2012).
- [87] A. Karplus and K. Diederichs, Linking crystallographic model and data quality, *Science* **336**, 1030 (2012).
- [88] A. Karplus and K. Diederichs, Assessing and maximizing data quality in macromolecular crystallography, *Curr. Opin. Struct. Biol.* **34**, 60 (2015).
- [89] J. M. Holton *et al.*, The R-factor gap in macromolecular crystallography: an untapped potential for insights on accurate structures, *FEBS J.* **281**, 4046 (2014).

Appendix A: Numerical Method

Simulating scattering off a protein from an XFEL pulse consists of two stages -

1. Solve equations (1) and (2) simultaneously to obtain the time-dependent probability distribution for the ionic states $P_\xi(t)$.
2. Perform a spatially-resolved Monte Carlo simulation of the elastic scattering pattern, with the ionic states of the atoms in the structure sampled from $P_\xi(t)$ at each discrete timestep.

1. Scattering pattern

The scattering pattern is calculated as [2, 30]

$$\langle I(q) \rangle = I_e(q) \int dt \Phi(t) \langle |F(t, q_j)|^2 \rangle, \quad (A1)$$

$$\text{where } I_e(q) = \frac{1}{2} r_e^2 (1 + \cos^2 2\theta) H_{\text{beam}}. \quad (A2)$$

Here, q_j is the momentum transfer corresponding to pixel j , H_{beam} is the fluence of the (unpolarized) incident beam, and r_e is the classical electron radius. $F(t, q_j)$ is defined by approximating each atom a as remaining fixed in its initial position R_a , with each form factor $f_a(t, q_j)$ (the Fourier transform of the atom's electron density) corresponding to a state ξ with probability $P_\xi^a(t)$, giving

$$F(t, q_j) \approx \sum_a f_a(t, q_j) \mathcal{T}_a(q_j), \quad (A3)$$

$$\text{where } \mathcal{T}_a(q_i) = \exp(-iq_i \cdot R_a). \quad (A4)$$

2. Cubic spline representation of the free electrons

The collision kernel on the right hand side of the Boltzmann equation, Equation (1), takes the form of a sum over distinct processes,

$$\begin{aligned} \mathcal{Q}[P_\xi, f](\epsilon) = & \mathcal{Q}^{\text{Photo}}[P_\xi](\epsilon) + \mathcal{Q}^{\text{Auger}}[P_\xi](\epsilon) + \mathcal{Q}^{\text{EI}}[f, P_\xi](\epsilon) \\ & + \mathcal{Q}^{\text{TBR}}[f, P_\xi](\epsilon) + \mathcal{Q}^{\text{EE}}[f](\epsilon) \end{aligned} \quad (A5)$$

The solution of these coupled rate equations presents serious numerical challenges:

1. The primary-ionization terms $\mathcal{Q}^{\text{Photo}}$ and $\mathcal{Q}^{\text{Auger}}$ are essentially Dirac delta-like source terms; such singularities often destabilize numerical PDE solutions.
2. The number of possible electron configurations scales factorially with the number of electrons in a given atom.

3. The three-body recombination term Q^{TBR} is quadratic in the free electron distribution f , leading to worst-case N^3 complexity if the representation of f is N dimensional.
4. The electron-electron recombination term Q^{EE} depends on derivatives of the free electron distribution.

We seek a representation for f that i) is inherently smooth and at least once differentiable, ii) is capable of representing strongly-peaked ionization functions without Gibbs-like phenomena, and iii) admits a computationally efficient representation of Q^{TBR} .

The standard approach [84] to non-LTE plasma simulation solves the Boltzmann equation using finite differencing of $f(\epsilon, t)$. We take a more general approach, expanding f with respect to a time-invariant basis $\mathcal{B} = \{\phi_i(\epsilon), i = 1 \dots N\}$, contracted with time-varying expansion coefficients $c^i(t)$ and multiplied by an explicit weight function $w(\epsilon)$,

$$f(\epsilon, t) = w(\epsilon) \sum_i c^i(t) \phi_i(\epsilon). \quad (\text{A6})$$

This expansion must be valid both at early times, when f resembles a sum of Dirac delta functions at the photoelectron and Auger electron energies, and at later times, when it resembles a Maxwell-Boltzmann distribution $f_T(\epsilon) \sim \sqrt{\epsilon} \exp(-\epsilon/k_B T)$. Typical orthogonal bases for $L^2(\mathbb{R})$ (e.g. Legendre polynomials, Fourier sines) are simple to differentiate and suitable for describing the smooth features of a Maxwellian, but suffer from Gibbs' phenomena in the vicinity of the strongly peaked atomic lines. The other typical basis choice – the orthogonal rectangles of finite-element analysis – works well when describing sharp peaks, but is susceptible to numerical instabilities when calculating derivatives [61].

Order- k B-splines ($k = 3$ in this work) are a good compromise between the two approaches. A collection of N splines of order k is defined over a grid of non-decreasing ‘knot points’ that collectively form the *knot vector* $T = \{t_j | j = 0 \dots N+k-1, t_k \geq t_{k-1}\}$ [68]. An expansion f constructed from order- k B-splines is automatically polynomial away from the knots, and at a knot point of multiplicity m has $k-1-m$ continuous derivatives. The knot vector is constructed such that the first and last knots have multiplicity k , while all interior points are distinct. With this choice of knot vector, the ϕ_k form a partition of unity – $\forall x \in [t_0, t_{N+k-1}], \sum_n \phi_n(x) = 1$.

Such functions are not mutually orthogonal, possessing a non-trivial overlap matrix $S_{ij} := \int d\epsilon w(\epsilon) \phi_i(\epsilon) \phi_j(\epsilon)$. This basis permits an approximate representation of a narrow primary electron peak by a C^1 piecewise polynomial, ensuring that the distribution has a well-defined derivative everywhere. Eq. (1) may then be recast in a finite form by integrating both sides against a test basis element ϕ_j ,

$$\int d\epsilon \phi_j(\epsilon) \frac{\partial f(\epsilon, t)}{\partial t} = \int d\epsilon \phi_j(\epsilon) Q[P, f](\epsilon, t) \quad (\text{A7})$$

$$\Rightarrow S_{ij} \frac{dc^i(t)}{\partial t} = Q_j[P, f](\epsilon, t), \quad (\text{A8})$$

which has the added benefit of rendering the Q tensors sparse.

In our approximation scheme, we assume

1. Purely (semi)classical collisional dynamics,
2. Independent, decoupled atoms,
3. Spatial homogeneity.

Assumption 2) is equivalent to discarding second-order and higher correlations in the electrons’ distribution function.

The first-order electron density function has two components – $f(\epsilon, t)d\epsilon$, the continuum energy distribution of the free continuum, and $P_\xi(t)$, the time-dependent density of ions in atomic configuration $\xi \in \{1s^2 2s^2, 2s^2, \dots\}$.

We separated the time-dependent energy distribution of free electrons $f(\epsilon, t)$ from the discrete probability distribution $P_\xi(t)$ capturing the classical populations of each atomic state ξ . The Boltzmann and master equations (1) and (2) then generate a deterministic time evolution of the electrons’ classical energy-state distribution.

Further numerical methods employed included: (I) An asynchronous implicit-explicit (IMEX) method, stepping the stiff but computationally cheap free electron interactions with much shorter steps than the bound-bound and bound-free contributions. (II) Adaptive time steps to avoid divergence in $f(\epsilon, t)$.

3. Explicit form of numerical couplings

We adopt the following notation:

a : Index for atom types, e.g. C,N,O,...

ξ, η : Indices for electron configurations of a particular atom type

$\Gamma_{\xi \rightarrow \eta}$: Transition rate from configuration ξ to configuration η . Square brackets indicate an f -dependent decay rate.

$B_{\xi\eta}$: Difference in total binding energy between electron configurations, $B_\xi - B_\eta$

a. Electron-Electron interactions

We model the Coulomb-mediated relaxation of the electron gas using a standard Fokker-Planck kernel, specifically the form quoted by Ref. [61],

$$\mathcal{Q}^{ee}[f](\epsilon) = -\frac{\partial J^{ee}[f](\epsilon)}{\partial \epsilon}, \quad (\text{A9})$$

where the electron current J^{ee} has the form

$$J^{ee}(\epsilon) = \alpha \left[F(\epsilon, t) \left(\frac{f}{2\epsilon} - \frac{\partial f}{\partial \epsilon} \right) - G(\epsilon, t) f \right], \quad (\text{A10})$$

$$F(\epsilon, t) = 2\epsilon^{-1/2} \int_0^\epsilon x f(x, t) dx + 2\epsilon \int_\epsilon^\infty x^{-1/2} f(x, t) dx, \quad (\text{A11})$$

$$G(\epsilon, t) = 3\epsilon^{-1/2} \int_0^\epsilon f(x, t) dx, \quad (\text{A12})$$

$$\alpha = \frac{2}{3} \pi e^4 (2/m)^{1/2} \ln \Lambda. \quad (\text{A13})$$

Notice that the electron-electron interaction strength requires an estimate of the Coulomb logarithm $\ln \Lambda = \int d\chi/\chi$ [57, 84, 85]. In our case, we cut the integral off using the Debye length and radius of closest approach $r_0 = e^2/4\pi\epsilon_0 k_B T$, giving $\Lambda = n4\pi\lambda_D^{-3}$ [85]. The temperature T here represents the notional temperature of the thermalized free electrons, estimated by a dynamical fit to the Maxwellian portion of the distribution.

b. Photoionization and Auger decay

Both processes produce primary electron emission spectra with very narrow linewidths. For numerical stability, we artificially broaden these features into a linear combination of the two basis splines nearest the desired energy, with coefficients chosen such that

$$\int d\epsilon \Delta_E(\epsilon) = 1, \quad \int d\epsilon \Delta_E(\epsilon) \epsilon = E. \quad (\text{A14})$$

This approach avoids introducing spurious negative-density parts to the distribution, as would be the case if a naive expansion of $\delta(E - \epsilon)$ were used. This should be a mild approximation in the XFEL regime, as the semi-empirical estimate of Ref. [61] indicates such broadening occurs on a subfemtosecond timescale.

$$\mathcal{Q}_a^{\text{Pht}}[P_a](\epsilon, t) = \sum_{\xi \in \mathcal{C}_a} P_\xi(t) \sum_{\eta \neq \xi} \Delta_{\hbar\omega - B_{\xi\eta}}(\epsilon) \Gamma_{\xi \rightarrow \eta}^{\text{Pht}} \quad (\text{A15})$$

$$\mathcal{Q}_a^{\text{Auger}}[P_a](\epsilon, t) = \sum_{\xi \in \mathcal{C}_a} P_\xi(t) \sum_{\eta \neq \xi} \Delta_{B_{\xi\eta}}(\epsilon) \Gamma_{\xi \rightarrow \eta}^{\text{Auger}} \quad (\text{A16})$$

c. bound-free interactions

Expressions for $\mathcal{Q}_a^{\text{EII}}$ and $\mathcal{Q}_a^{\text{TBR}}$ were derived according to the work of Ref. [54], to which we direct the reader.

4. Dynamic grid implementation

The plasma code's cubic spline treatment has previously been shown to well-approximate the evolution of relatively static Boltzmann-governed systems with as few as 10 energy grid points/knots [86]. However, this requirement grew by an order of magnitude when the initial distribution of particles was modestly (relative to the energy scale of the present work) displaced from equilibrium with a thermal bath. The unbound electron continuum of a biological target under XFEL illumination sees an acute difference between its state at early times and its partially equilibrated state near the end of the pulse. Moreover, these systems see two complications not present in the systems considered by Khurana *et al.*: (I) The narrow, low-energy peak of the Maxwellian at early times is difficult to fit due to the rigid energy conservation condition of $\frac{df}{d\epsilon^2} \approx 0$. (II) The thermal bath is substituted for sharp, high-energy emission profiles, which, like the Maxwellian, shift significantly over the course of the pulse as they relax through electron interactions [34].

An adaptive grid was implemented to address these issues. A set of static low-density regions spans the full energy range and a set of *dynamic* high-density regions spans (I) the Maxwellian and (II) up to 4 of the most dominant high-energy peaks. We define a set of energy ranges (regions), each with an associated knot density function $\xi(\epsilon)$ that is only non-zero within the region. The local knot density of the full grid $\Xi(\epsilon)$ is then defined as

$$\Xi(\epsilon) = \max(\xi_1, \xi_2, \dots, \xi_{n-1}, \xi_n). \quad (\text{A17})$$

The high-density regions of the electron continuum are dynamically updated throughout the simulation to follow their respective features. A high density of knots supports the sharp features in the continuum at early times, then redistribute to continue to support the growing and shifting peaks as the electron population equilibrates. Accurate fitting of the continuum at early times appears to be particularly crucial, so a partial run of the simulation with a ‘guess grid’ is used to obtain the initial grid for the actual simulation. This flexible approach drastically reduced the number of knots necessary to achieve convergence in the evolution of the ionic states.

The spline basis is transformed with a 64-point Gaussian quadrature. Transformations in the simulations of this work were all performed an order of 10 times. Testing found the convergence to be independent of the associated error for >100 transformations. The photoelectron peaks were identified dynamically based on their maximum energy density relative to the transition energy region, without regard for the prior basis.

Appendix B: R_{dmg}

The standard theoretical measure of electronic damage [2] is

$$R_{dmg} = \frac{\sum_q |\sqrt{I_{\text{ideal}}(q)} - \sqrt{I_{\text{real}}(q)}|}{\sum_q \sqrt{I_{\text{ideal}}(q)}}, \quad (\text{B1})$$

where q is the momentum transfer corresponding to a pixel (in some other studies, the Bragg peak), and $I_{\text{ideal}}(q)$ and $I_{\text{real}}(q)$ are the normalized irradiances scattered by the system in the cases where electronic damage is, respectively, ignored or included.

We note that the ‘rule of thumb’ that $R_{dmg} < 0.15$ – 0.20 implies a recoverable structure [2, 20, 29, 32] is difficult to reconcile with certain experimental concerns. The essence of this matter may be distilled into two points. (I) The original introduction of a notional cutoff was predicated on R_{dmg} being an achievable limit for the experimental measure of deviation within the merged dataset (R_{merge}) [2]. However, data quality R factors are not predictive of refinement quality [87, 88]. (II) R_{dmg} measures only damage-induced noise, while experimental R factors account for all sources of noise. Both R_{merge} and the standard refinement measure R_{free} are mostly confined to a value range of ~ 0.10 across macromolecules deposited in the Protein Data Bank [2, 89], so it is ill justified to discount a single source of noise which in isolation produces an R factor on the same order—at least not without experimental support.

Even in the regime where radiation damage is minimal and R_{dmg} would be near 0, an R_{free} below 0.15 is rarely seen in refined models of macromolecules [89]. The confounding factors responsible for this difficulty may be magnified by radiation damage, making a cutoff based solely on trends in R factors of deposited structures ill-defined. This suggests that a cutoff for R_{dmg} that reliably gauges the limit of tolerable damage in SFX would need to be informed by (presently lacking) empirical data on how damage impacts R_{free} .

Appendix C: Influence of cascade energy with controlled seeding rate

Increasing the X-ray energy above an absorption edge decreases the photoabsorption coefficient, but also raises the energy of its seeded cascades. To isolate the relationship between a cascade’s energy and the damage it causes, AC4DC was modified to model the ionization of the light-atom control with additional electrons injected at a rate independent of their energy, under a Gaussian 10^{12} 10 keV $\text{ph}\cdot\mu\text{m}^{-2}$, 15.0 fs FWHM pulse. The injection rate was fixed at three times the photoionization

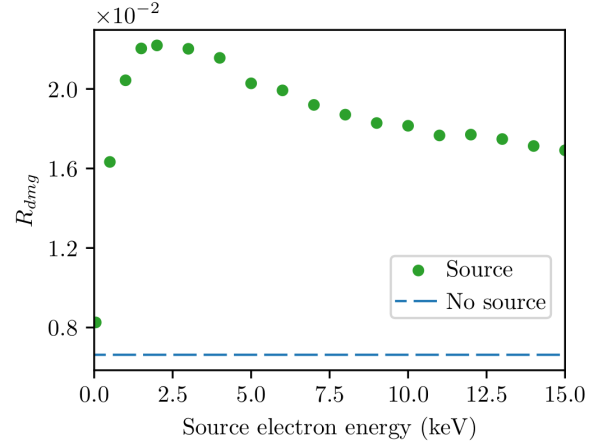


FIG. 11. Energy-dependence of damage induced by electrons seeded in a light-atom target. Each dot corresponds to a simulation of the light-atom control subjected to a 10^{12} 10 keV $\text{ph}\cdot\mu\text{m}^{-2}$, 15.0 fs FWHM pulse, but with an artificial injection of free electrons at the energy denoted by the horizontal axis. Electrons were injected at three times the rate of the neutral target’s photoionization rate for a given intensity. The dashed line indicates the value of R_{dmg} when no electrons are injected.

rate of the *undamaged* target for a given incident intensity, coarsely corresponding to the ionization rate of the Zn-doped lysozyme by its Zn ions under the same pulse conditions. (Zn was chosen due to showing a particularly distinct local maximum above its K-edge.) The resulting relationship between the electron source energy and the damage suffered by the target (Fig. 11) shows strong similarities to the relationship between LPE and damage in the Zn-doped target shown in Fig. 7(b). Notably, showing a local maximum at a similar position and magnitude.

Appendix D: Supplementary Figures

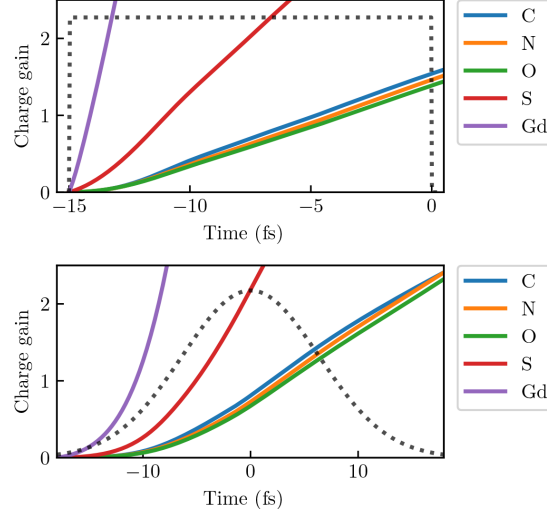


FIG. S1. Effect of the choice of pulse profile used in simulating the dynamics of ‘continuous’ lysozyme.Gd in Sec. III. Plots show the evolution of the elements’ average charges under the Gaussian and square pulse profile idealizations for a 15 fs FWHM pulse, as represented by the dotted lines. By $t = 0$, the target is in a more ionized state under the Gaussian pulse. Both pulses used a fluence of 1.75×10^{12} 7.112 keV ph· μm^{-2} .

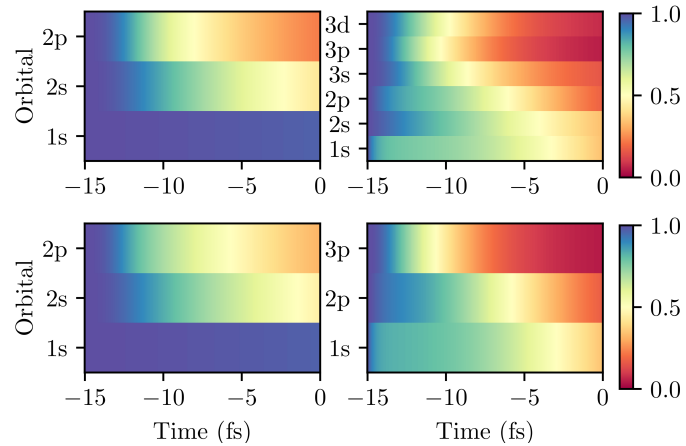


FIG. S2. Occupancy of C and Fe within the Fe-doped protein, with (top) and without (bottom) the single-shell approximation that was applied in this study to atoms heavier than Fe. The pulse was modeled with a 15 fs square temporal profile, and a fluence of 10^{13} 10 keV ph· μm^{-2} . TBR was disabled in these simulations. The approximation has a negligible impact on the target’s ionization.

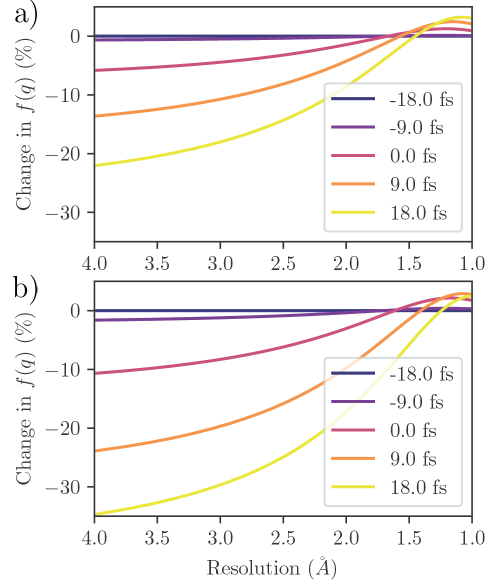


FIG. S3. Evolution of the scattering amplitude of carbon atoms in lysozyme.Gd as a function of the scattering angle, under the illumination conditions of Sec. III. (a) Simulation with only light atoms. (b) Simulation with all atoms. Traces correspond to the ‘average’ carbon atom in the protein at the denoted times, defined as a carbon atom with the average orbital occupancies of all carbon atoms. The atomic form factor $f(q)$, where q is the momentum transfer, is defined as the Fourier transform of the atom’s electron density. The vertical axis gives the change in $f(q)$ for the average carbon atom relative to the form factor of a carbon atom in its neutral ground state. The horizontal axis gives the resolution ($2\pi/q$) corresponding to the scattering angle.

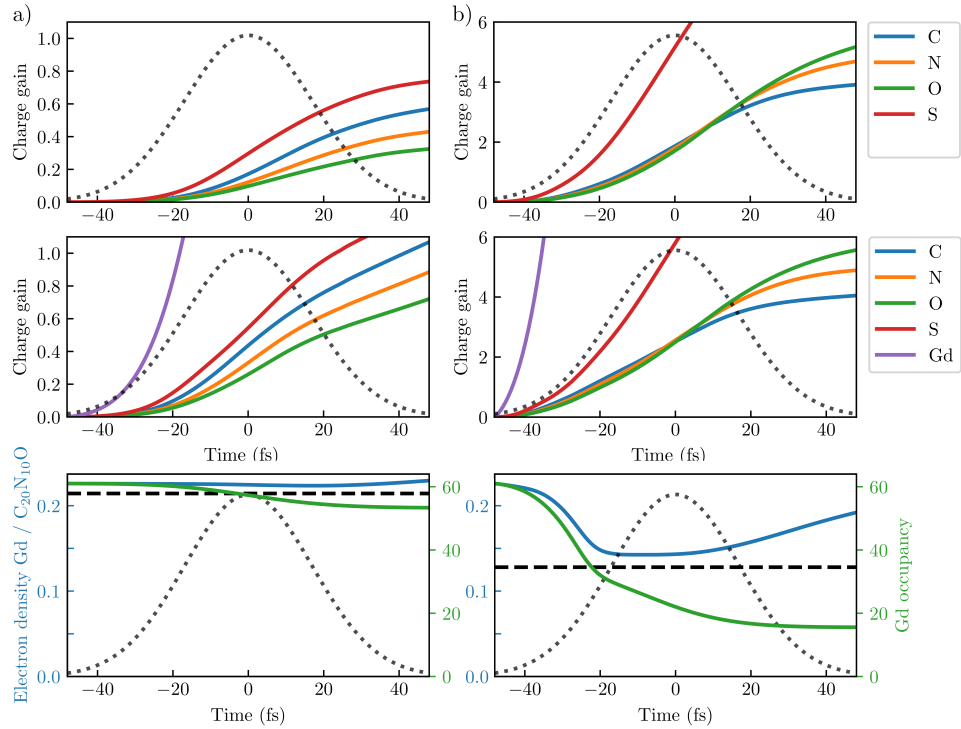


FIG. S4. Effect of Gd ions on the ionization of lysozyme.Gd in the (a) low and (b) high fluence experiments performed by Ref. [47]. Pulses were simulated with 40 fs FWHM Gaussian profiles, and (a) 1.3×10^{11} 8.48 keV $\text{ph}\cdot\mu\text{m}^{-2}$ or (b) 7.8×10^{12} 8.48 keV $\text{ph}\cdot\mu\text{m}^{-2}$ fluence. The photon energy is above the L-edge of Gd (modeled as 7.42 keV). Plots in the top row correspond to simulations with Gd excluded. The presence of Gd ions (middle row) increases the ionization of the light atoms. Plots in the bottom row show the evolution of the Gd occupancy and EDR. The horizontal dashed line shows the EDR based on the ionization expected in each element by the original study. Note that Gd occupancy is proportional to EDR neglecting light atom damage.